Journal of Alloys and Compounds 725 (2017) 783–791

Contents lists available at ScienceDirect

Journal of Alloys and Compounds

journal homepage: http://www.elsevier.com/locate/jalcom

Dependences of phase stability and thermoelectric properties of type-I clathrate $Ba_8Cu_{4.5}Si_6Ge_{35.5}$ on synthesis process parameters

X. Yan [a], [*], A. Prokofiev [a], E. Bauer [a], [d], P. Rogl [b], J. Bernardi [c], S. Paschen [a], [**]

[a] Institute of Solid State Physics, Vienna University of Technology, Wiedner Hauptstr. 8–10, 1040 Vienna, Austria
[b] Institute of Materials Chemistry and Research, Vienna University, Währingerstr. 42, 1090 Vienna, Austria
[c] USTEM, Wiedner Hauptstr. 8-10, 1040 Vienna, Austria
[d] Christian Doppler Laboratory for Thermoelectricity, TU Wien, Wiedner Hauptstr. 8–10, 1040 Vienna, Austria

ARTICLE INFO

Article history:
Received 12 May 2017
Received in revised form
18 July 2017
Accepted 21 July 2017
Available online 22 July 2017

Keywords:
Thermoelectric properties
Ball milling and hot pressing
Clathrates
Microstructure

ABSTRACT

Thermoelectric materials are actively considered for waste heat recovery applications. To improve the thermoelectric (TE) performance, nanostructuring to reduce their thermal conductivity has been inferred as an effective approach. Here, we present our investigations of the influence of ball milling and hot pressing process parameters on the chemical and thermoelectric properties of the type-I clathrate $Ba_8Cu_{4.5}Si_6Ge_{35.5}$. Powders with very small grain sizes could be obtained by ball milling. However, in contrast to other materials, the ultra-fine powders deteriorate the sintering behavior in the hot pressing process. We suggest that this is mainly due to an oxygen-induced local decomposition of the clathrate phase, which might start from the surface of nanoparticles. Partial decomposition also occurs in sintered samples of low bulk density when they are heated under low vacuum conditions. Overall this leads to the loss of Si/Ge and thus to an enhanced Cu content in the remaining clathrate(s), which deteriorates the TE performance in spite of the reduced thermal conductivity. Thus, keeping the composition and structure of the clathrate stable during the nanostructuring process is essential for reaching high TE performance.

1. Introduction

Thermoelectric (TE) materials continue to attract great interest since they are able to convert waste heat to electricity. Although the employment of these materials for energy conversion offers many advantages compared to conventional methods, TE materials currently fill only niche applications. The main limitation arises from the low dimensionless thermoelectric figure of merit $ZT = TS^2/(\rho\kappa)$, where T, S, ρ, and κ are the absolute temperature, Seebeck coefficient, electrical resistivity, and thermal conductivity, respectively. To obtain high ZT is challenging because of the mutual interplay of S, ρ, and κ via the charge carrier concentration. Therefore, much effort has been devoted to the search for new concepts/theories, new technologies, and advanced materials with enhanced power factor S^2/ρ and/or reduced κ [1]. The most promising materials include nanostructured materials, structurally complex materials, and materials with unusual phonon modes [1–6].

Intermetallic type-I clathrates have been investigated extensively as promising thermoelectric materials because of their intrinsically low thermal conductivity [2,7–12], which arises from the unique crystal structure constructed by face-sharing cages. The cages are formed by covalently bonded IVA elements and filled by alkali or alkaline-earth elements [7,12]. The fillers (guest atoms) bond to the cage (framework) atoms only loosely and rattle in the cages [13,14]. This is responsible for the low thermal conductivity [13–16]. On the other hand, the framework atoms can be replaced by different atoms, providing opportunities to optimize the charge carrier concentration for high TE performance [12,17–19]. However, in a given system, concentration tuning is limited by the finite solid solubility of the substituting element. Thus, competitive ZT values in single crystals have only been obtained in relatively few cases so far [20–23]. Therefore, further reducing the thermal conductivity by micro- and/or nanostructuring [1,3–6,24] without degrading the power factor has proven to be a promising strategy.

Approaches to synthesize nanostructured materials involve bottom-up and top-down processes [25], of which ball milling (BM) as a top-down process has been demonstrated to be simple,

---

[*] Corresponding author.
[**] Corresponding author.

E-mail addresses: yan@ifp.tuwien.ac.at (X. Yan), paschen@ifp.tuwien.ac.at (S. Paschen).

http://dx.doi.org/10.1016/j.jallcom.2017.07.210
0925-8388/© 2017 Elsevier B.V. All rights reserved.

economic, and efficient [26–29]. This technique has frequently been used in different metal/intermetallic systems [26–31]. Basically, the fine particles are produced through accumulating dislocations in materials from severe plastic deformation during BM. Therefore, the grain size depends on the process parameters including the input energy for milling, the milling time, and the mechanical properties of the material [30–34]. Furthermore, the process parameters affect the chemical properties of the composition, defects, and phase constitutions as well as the mechanical properties such as the compressive yield strength and Vickers hardness in the final products [26–29].

BM inevitably introduces contaminations in the nanopowders, which can arise from the milling media material and/or from reactions of nanopowders with atmosphere [30,31]. These contaminations can influence the properties of the nanopowders and the sintering behavior. The properties of the sintered materials then get degraded. Thus, contaminations should be reduced to the lowest level in order to obtain very dense sintered samples, e.g., using inert gas during the BM process [35,36].

There are various methods for powder consolidation including conventional (pressureless) sintering, pressure-assisted sintering such as hot pressing (HP), spark plasma sintering, hot isostatic pressing, ultrahigh-pressure sintering, as well as more unconventional sintering approaches such as microwave heating [30]. The ultimate goal of these methods is to obtain very dense bulk materials with grain sizes on the nanometre-scale via controlling the process parameters of each method.

In our previous study on type-I clathrates in the system Ba-Cu-Ge-Si we showed interesting Si-content dependent thermoelectric properties [37]. Better thermoelectric performance was found in samples with lower Si content. We concluded in that study that the performance could be further improved if we could lower the thermal conductivity. Therefore, here we investigate the influence of process variables for BM and HP on the microstructure, composition stability, and TE properties of a model type-I clathrate with nominal composition $Ba_8Cu_{4.5}Si_6Ge_{35.5}$. The Cu content of this composition is lower than that in the optimized bulk composition [37]. This is because residual defects such as dislocations, voids, and boundaries in nanostructured samples trap electrons and then reduce the charge carrier concentration [38,39], whereas lowering the Cu content can increase the charge carrier concentration [40,41]. Thus, we expected that the optimum charge carrier concentration could be still attained in these nanostructured clathrates.

2. Experimental details

2.1. Sample preparation and characterization

More than 15 large samples (4 g each) of the same nominal composition $Ba_8Cu_{4.5}Ge_{35.5}Si_6$ were prepared in a high-frequency induction furnace from high-purity elements (>99.999 wt.% for Cu, Ge, and Si; >99.7 wt.% for Ba). The as-cast ingots were annealed at 800°C for 20 days (denoted as annealed samples), then ball milled in a Fritsch planetary mill. The process parameters for BM are given in Table 1. We fixed the weight ratio of ball to powder $R_{B/P}$ and the planetary ratio R_p according to our previous investigation [42]. In view of the brittleness of the clathrate samples, we selected a low speed for the main disk to study the grain size as a function of milling time t_m. The process was thus interrupted in every 2–4 h to pick up powders for characterizations and simultaneously, to separate the adhered powders from the milling media. The powders with different t_m were denoted as 1st-Ps and the final powders after $t_m = 19$ h were denoted as P-I. For comparison and confirmation of the usefulness of these process parameters, we also prepared powders using the same milling power and $t_m = 14$ h, but without interruption. These powders were denoted as P-II.

Table 1
Process parameters for ball milling, i.e., the mill type, the speed of the main disk, V_M (r/min), the ball to powder weight ratio, $R_{B/P}$, the planetary ratio, R_p, the material of containers and balls, and the size of the balls, S_B (cm). The milling time, t_m, is a process variable.

Type	V_M	$R_{B/P}$	R_p	Mater.	S_B
Pulverisette 7	120	80	−2.5	WC	1

We annealed the P-I powders at different temperatures (T_{AN}) to study the grain growth. The finding guides the temperature-setting for hot pressing. In the meantime, by comparing the grain sizes of the annealed powders with that of the sintered ones, we derived the role of pressure on size growth. Thus we set the annealing time of 2 h, i.e., the time for hot pressing (see below), to keep conditions for both processes as similar as possible.

Both P-I and P-II were loaded in a graphite die and hot pressed in an FCT hot-press system. A pressure of $p = 56$ MPa was applied at the beginning. The die was then heated in vacuum to 450°C and kept at this temperature for 30 min. Subsequently, the chamber was filled with Ar and the die was heated at a rate of 5 °C/min to the hot pressing temperature, T_p (Table 2). After 2 h the pressure was released and the die was cooled down in the system. The sintered sample was denoted by series number, HP, and T_p, e.g., IHP550.

X-ray powder diffraction (XPD) data were collected using a HUBER-Guinier image plate system (Cu $K_{\alpha 1}$, $8° \leq 2\theta \leq 100°$) in air at room temperature. Lattice parameters were calculated by least-squares fits to indexed 2θ values employing Ge ($a_{Ge} = 0.5657906$ nm) as internal standard. The crystallite size and the residual strain were evaluated from the peak broadening of the XPD pattern in the whole Bragg-angle range by using the MDI jade 6.0 software. For more technique details on the evaluation one can refer to Refs. [43,44] and the manual of the software. Annealed (300°C, 1 day) pure Si powder was used to estimate the peak broadening due to the X-ray instrument. The bulk density of the sintered (hot pressed) samples was measured by the Archimedes method.

The composition of the clathrate phase and the microstructure of the hot pressed samples were checked by energy dispersive X-ray spectroscopy (EDX) in a scanning electron microscope (SEM) operated at 20 kV (Zeiss Supra 55VP, probe size: 1μm). The grain sizes of selected powders/samples were estimated by measuring the grain dimensions within the microstructure images from transmission electron microscopy (TEM).

2.2. Transport property measurements

The electrical resistivity and Seebeck coefficient were measured with a ZEM-3 (ULVAC-Riko, Japan) in a temperature range from room temperature to 600°C. The thermal conductivity was calculated from the thermal diffusivity D_t, measured with a laser flash method with a Flashline-3000 (ANTER, USA), the specific heat C_p, and the bulk density D using the relation $\kappa = D_t C_p D$. C_p was measured in a comparative procedure in the Flashline-3000, using NIST steel as reference.

Below room temperature the thermal conductivity was obtained by a steady state heat flow method on rectangular samples with a cross section of 1–2 mm^2. The temperature gradient along the samples was determined by a differential Au/0.07%Fe versus Chromel thermocouple and the absolute temperature was measured by a Ge resistor below and a Pt resistor above 40 K, respectively. Three concentric radiation shields were mounted around the sample to reduce the radiation losses during the measurement.

Table 2
Grain size S_g measured by TEM, crystallite size S_c and residual strain ε evaluated from XPD, relative density D_r and lattice parameters a for samples pressed from the P-I samples (IHP) and from the P-II samples (IIHP) at different pressing temperatures T_p.

T_p(°C)		550	600	650	700
IHP	S_g (nm)	25–35	30–40	–	35–45
	S_c (nm)	23.3(2)	24.0(2)	–	28.1(3)
	ε (%)	0.042(4)	0.036(4)	–	0.069(3)
	D_r (%)	69(2)	70(2)	–	74(4)
	a (nm)	1.06383(3)	1.06476(5)	–	1.06662(4)
IIHP	S_c (nm)	91.1(6)	94.9(3)	105.2(1)	113(1)
	ε (%)	0.080(1)	0.051(1)	0.030(1)	0.024(1)
	D_r (%)	70.4(2)	75.7(6)	80.9(4)	93.3(3)
	a (nm)	1.06433(3)	1.06407(2)	1.06436(1)	1.06421(2)
T_p(°C)		720	740	760	800/780
IHP	S_g (nm)	–	–	–	100–150
	S_c (nm)	–	–	–	122(2)
	ε (%)	–	–	–	0.048(1)
	D_r (%)	–	–	–	92(2)
	a (nm)	–	–	–	1.06704(2)
IIHP	S_c (nm)	113(2)	131(3)	137(3)	147(3)
	ε (%)	0.029(1)	0.025(1)	0.014(1)	0.022(1)
	D_r (%)	94.9(4)	96.3(5)	99.2(3)	99.3(4)
	A (nm)	1.06433(2)	1.06443(2)	1.06427(1)	1.06411(1)

The measurement uncertainties are 2% for the electrical resistivity and Seebeck coefficient and 5% for the thermal conductivity at low temperatures and 7–10% at high temperatures.

3. Results

3.1. Microstructure evolution

Fig. 1 shows the XPD patterns of an annealed sample as well as that of milled-powders (the 1st-Ps powders) with different milling times t_m. The major peaks can be indexed by the type-I clathrate phase, and the remaining weak peaks can be indexed by the diamond Ge(Si) phase. The phase constituents in all samples were further confirmed by EDX measurements. With increasing t_m, peak broadening is observed in the powder patterns (see the inset of Fig. 1, the patterns are from the same exposure time and without normalization). This indicates that the grain sizes in powders get smaller and the residual strain get larger with t_m. The peak positions of the clathrate phase, however, do not change with t_m, implying that no change in phase composition occurs during the ball milling process. Also, no obvious evidence for the formation of an amorphous phase and/or oxides in powders, even in the sample after 19 h milling, is seen from these patterns.

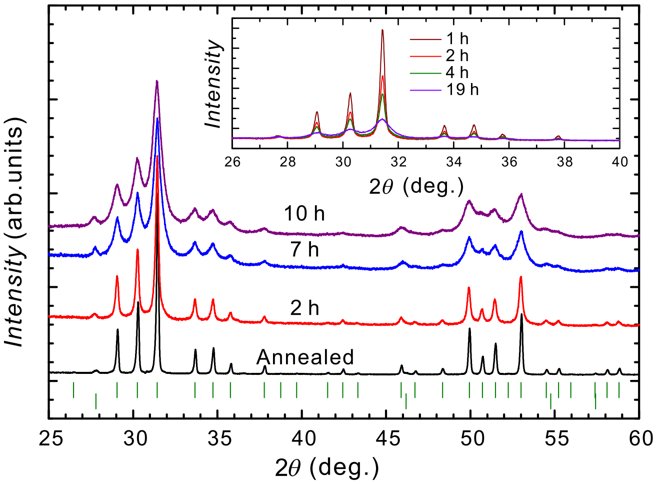

Fig. 1. XPD patterns of an annealed sample and as milled powders (1st-P) with different milling time t_m. The patterns are normalized to the highest peak of the type-I clathrate phase. The vertical lines (dark green) at the bottom denote the Bragg positions of the clathrate and diamond phases. The inset shows the non-normalized patterns of the powders recorded with the same X-ray exposure time. (For interpretation of the references to colour in this figure legend, the reader is referred to the web version of this article.)

The crystallite size S_c and residual strain ε as a function of t_m are shown in Fig. 2. As in other brittle materials, S_c decreases rapidly at the beginning of the process and starts to saturate after 10 h. A minimum size of about 18(1) nm is reached in P-I. ε first increases, remains roughly constant after $t_m = 7$ h, and finally decreases slightly with further milling.

By comparison, the S_c of 45(5) nm for the P-II powders is higher than that of the P-I powders, while ε is very similar (Fig. 2(a)). Comparing the crystalline size of 45(5) nm with the curve of Fig. 2(a), left, milling effective for size reduction has apparently stopped after 5 h. Thus, a separation for the agglomerated powders and the adhered powders on the milling media, as done in the 1st-Ps powders, is crucial for keeping the milling process effective. A possible approach to against agglomeration is to use agents, which can be selected with no chemical influences on the matrix material and can be easily removed during the sintering processes [45,46].

The average grain sizes of P-I measured by TEM are similar to the crystallite sizes S_c (Table 2). Fig. 3(A) shows the TEM image of powders with $t_m = 7$ h, as an example. The grain size ranges from few nanometres to several 100 nm. Similar size dispersions were also seen in other powders of different t_m. Powders with a longer t_m have a narrower size distribution. Electron diffraction investigations (not shown) reveal that all imaged grains crystallize very well, confirming the absence of an amorphous phase in powders.

Fig. 2(b) shows S_c and ε versus annealing temperature T_{AN}. An increase of S_c starts at 500°C and becomes rapid beyond 600°C. The release of ε starts at 250°C and is essentially complete at 500°C. This indicates that the absorbed heat energy is used first to release the residual strain and then for the grain growth. This suggests that a hot pressing temperature of 500°C to 600°C could sinter powders into mechanically stable but still nanostructured bulk samples.

In all sintered samples, the residual strain is similar and very small (Table 2), while the grain/crystallite size generally increases with increasing T_p (Fig. 2(b)). The sizes in IHP are smaller than in

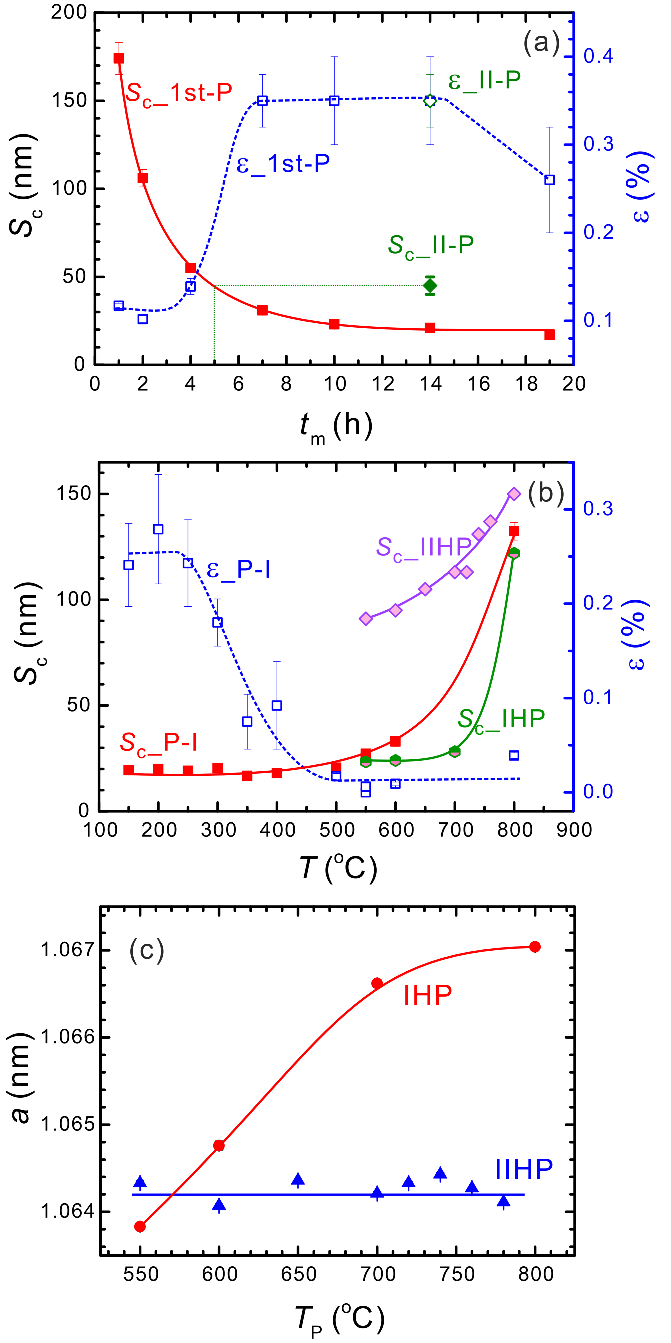

Fig. 2. (a) Changes of crystalline size (red solid square) S_c and residual strain (blue empty square) ε with the milling time t_m for the first series of powders 1st-P. The S_c (green solid diamond) and ε (green empty diamond) of P-II is plotted for comparison. The dotted line indicates that the actual milling time of 14 h of P-II corresponds to an effective milling time of only 5 h (see text); (b) changes of S_c and ε in I-P with annealing temperature T_{AN} (red solid square and blue empty square, respectively). The crystalline sizes of the IHP and IIHP samples as a function of hot pressing temperature T_P are also included for comparisons; (c) changes of the lattice parameter a with T_P for the IHP (red solid circle) and IIHP (blue solid triangle) samples. All lines behind data points are guides to the eye. (For interpretation of the references to colour in this figure legend, the reader is referred to the web version of this article.)

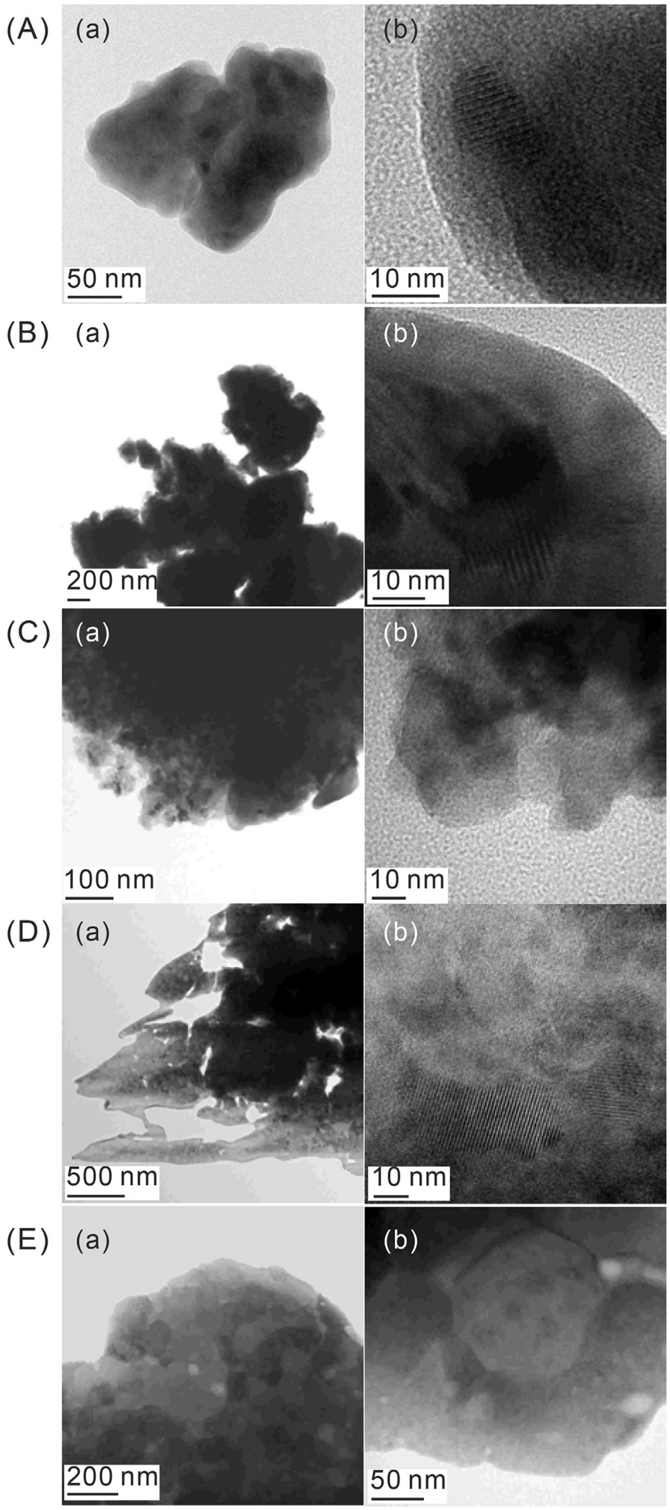

Fig. 3. Microstructure of samples from TEM measurements: (A), powders after 7 h milling; (B), IHP550; (C), IHP600; (D), IHP700; and (E), IHP800. (a) and (b) represent the low and high magnification, respectively.

IIHP under the same sintering conditions (the green line versus the violet line in Fig. 2(b)), which is related to the larger initial sizes in P-II. The sizes in IHP are also smaller than in the annealed powders where $T_p = T_{AN}$ (the green line versus the red line in Fig. 2(b)), which indicates that the pressure depresses the grain growth during hot pressing (the powders for annealing and the sintering of IHP come all from P-I).

The average grain size in IHP from TEM (Fig. 3(B)–(E)) is similar to the crystallite size from XPD. A size increase with increasing T_p can be observed in these samples.

The lattice parameter of the clathrate phase (Table 2) increases systematically with T_p in IHP but is almost constant in IIHP (see Fig. 2(c)). The change of lattice parameter reflects the change of the composition in IHP. While in IIHP, the composition is stable, independent of T_p.

From the microstructure images of both series of HP samples taken by SEM (Fig. 4), a systematic evolution of pores and dense areas with T_p can be seen. The sizes of the dense areas, which were formed by particle bonding during sintering, increase with increasing T_p. Consequently, a larger bulk density is reached in the sample with a higher T_p. The visible morphology difference between IHP700 and IIHP720 is consistent with the high bulk density measured in the latter sample (Table 2). It indicates that the bulk density of the sintered sample depends on not only the sintering temperature, but also the properties of the nanopowders.

3.2. Thermoelectric properties

Fig. 5 summarizes the thermoelectric properties of IHP and IIHP. Obvious differences in the temperature dependences of the transport properties are seen between the two series of samples. The IHP samples show semiconducting behavior, as the electrical resistivity ρ increases with decreasing temperature. At 300 K, ρ increases with increasing hot pressing temperature T_p up to 700°C, then it decreases. Large differences of $\rho(300\text{ K})$ are observed between IHP550 and IHP600, and between IHP700 and IHP800. The Seebeck coefficient S changes sign from negative to positive with increasing T_p and reaches values of the order of 100 μ V/K in all samples at the highest temperatures. The thermal conductivity κ is relatively low except for IHP800. All thermal conductivities are mainly dominated by the phonon contribution due to the high electrical resistivity. The figure of merit ZT is low and IHP550 has higher ZT below 700 K than the other samples due to the relatively lower $\rho(T)$ at the low temperature range. The semiconducting behavior is likely due to an increased Cu content (loss of Ba, Ge, Si) in the clathrate phase and possibly the formation of oxides on the grain surfaces (see below).

The variation of the thermoelectric properties in IIHP on T_p is rather monotonous. ρ decreases with increasing T_p and shows metal-like behavior for all samples. S is negative (except for some samples at high T) and changes systematically with T_p. κ is larger than that of the first series of IHP samples. Nevertheless, the relatively low ρ results in high ZT values, with the highest ZT approaching 0.45 at ~ 873K in IIHP780. The transport properties of this series of samples are largely controlled by the grain sizes, which are further demonstrated by the systematic changes of the lattice thermal conductivity κ_{ph} at low temperatures.

Fig. 6 shows $\kappa_{ph}(T)$ of IIHP550, IIHP700, and IIHP780 at the temperature range of 4.2–150 K. The electronic contribution was subtracted by using electrical resistivity ρ via the Wiedemann–-Franz law with $L_0 = 2.44 \times 10^{-8}$ (V/K)^2. The IIHP550 sample, which has the lowest grain sizes, has also the lowest $\kappa_{ph}(T)$ and its temperature dependence is similar to that of amorphous materials. The IIHP780 sample, which has the largest grain sizes, also shows the largest κ_{ph}. The peak at around 30 K in $\kappa_{ph}(T)$ is a characteristic of crystalline materials.

3.3. Composition stability

As mentioned above composition changes in IHP were observed during the hot pressing process, as reflected by the different lattice parameters (Table 2 and Fig. 2(c), red circles). Furthermore, from the XPD patterns of the IHP samples in Fig. 7(A), we see peak shifts accompanied by intensity changes of the diamond phase, indicating a partial decomposition during the hot pressing process. This might occur due to oxygen on the surface of grains adsorbed during the repeatedly interrupted BM process in the first series of powders, which reacts with elements (such as Ba) in the clathrate phase. It is speculated that the decomposition starts from the surface of grains/holes (or other types of defects) and extends gradually into the body of grains. The extension largely depends on the amount of adsorbed oxygen, the grain sizes, and the temperature for hot pressing or for transport measurements. The localized decomposition leads to an increased Ge content in the diamond phase and thus we observed shifted and strengthened peaks for the diamond phase in the IHP samples with a high T_p (Fig. 7(A)). This leads to an enhanced Cu content in the clathrate phase because of the loss of the other framework elements (especially Ge). The enhanced Cu content shifts the Fermi level from the conduction band to the energy gap or even to the top of the valence band [40]. We thus see sign changes in S and systematic changes in ρ with T_p in the IHP series samples. The change of ρ with T_p is obviously non-linear since the

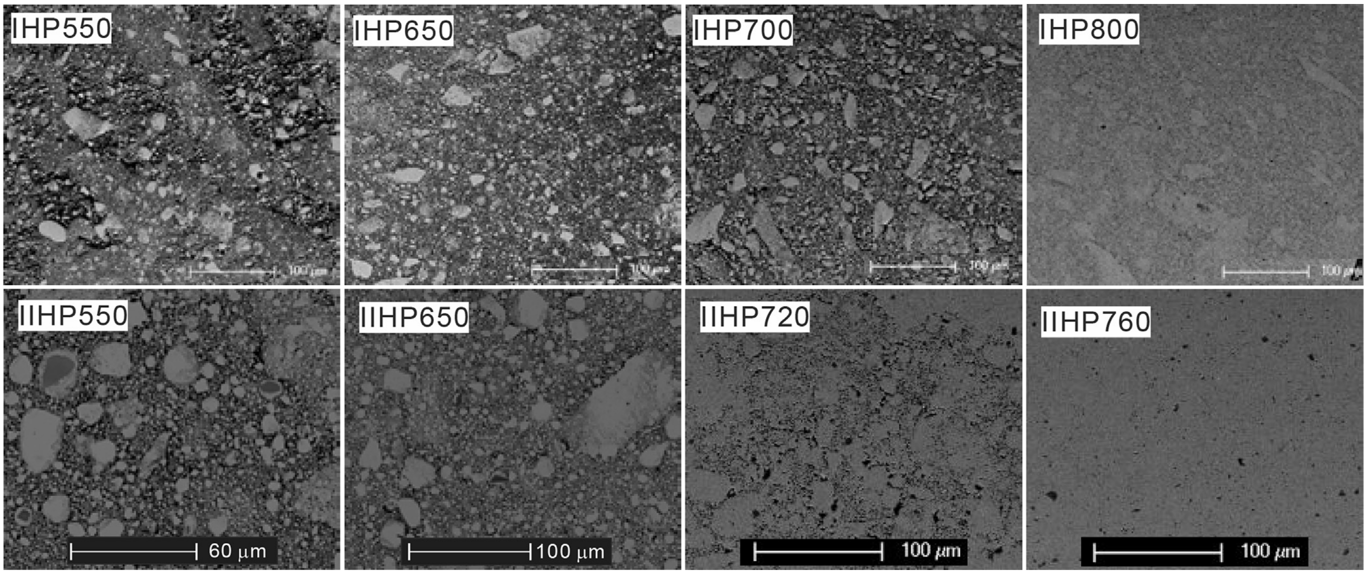

Fig. 4. SEM images of samples from both series (IHP and IIHP), hot pressed at different T_p.

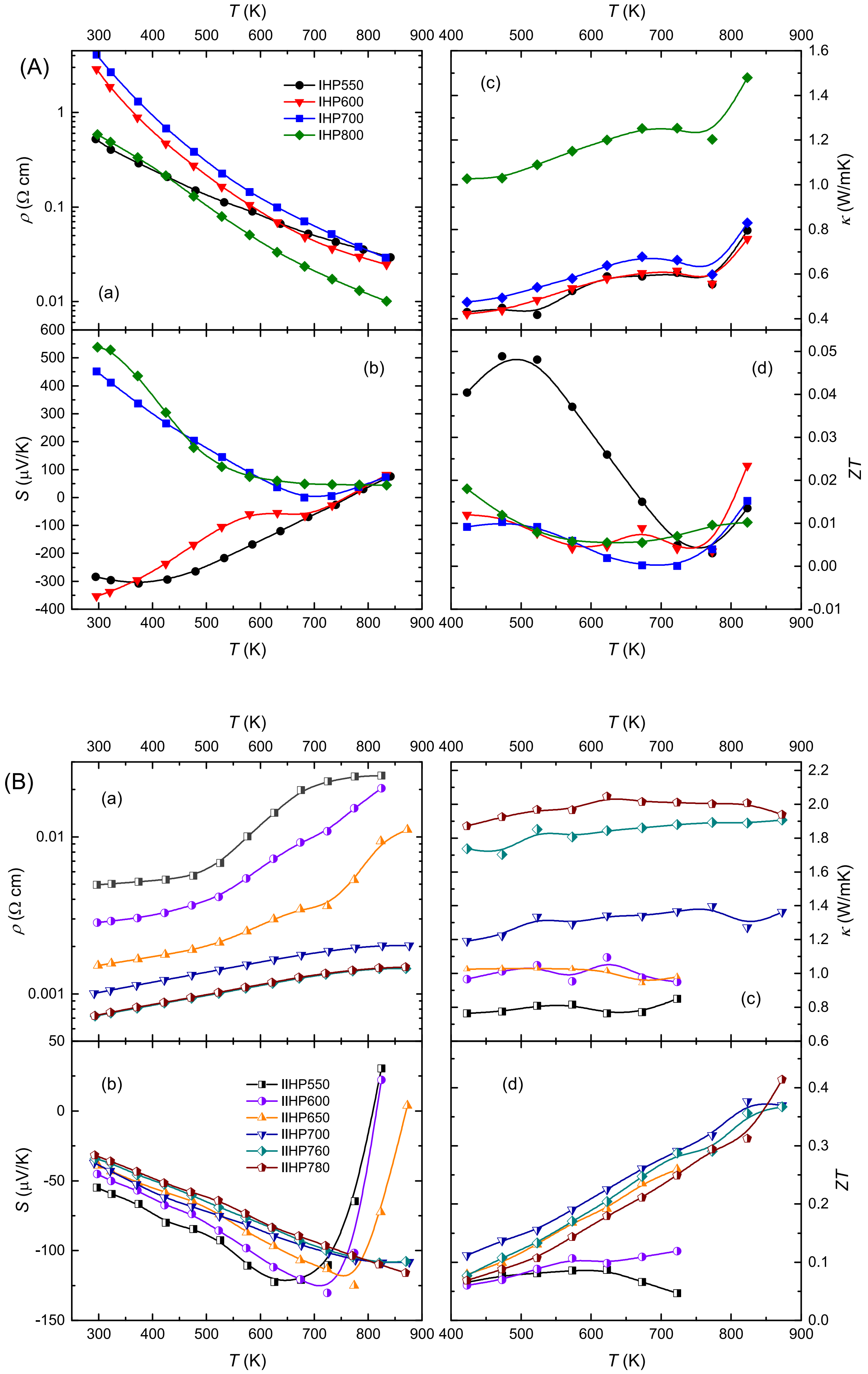

Fig. 5. Temperature dependent electrical resistivity $\rho(T)$ (a), Seebeck coefficient $S(T)$ (b), thermal conductivity $\kappa(T)$ (c), and figure of merit $ZT(T)$ (d) for samples of the IHP (A) and the IIHP (B) series.

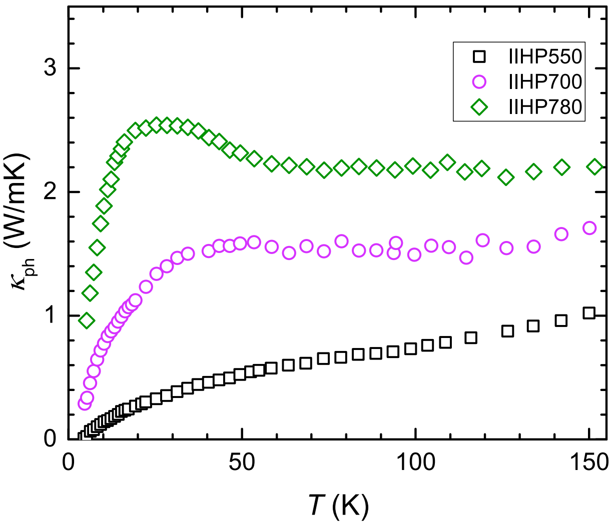

Fig. 6. Temperature dependent lattice thermal conductivity for IIHP550, IIHP700, and IIHP780.

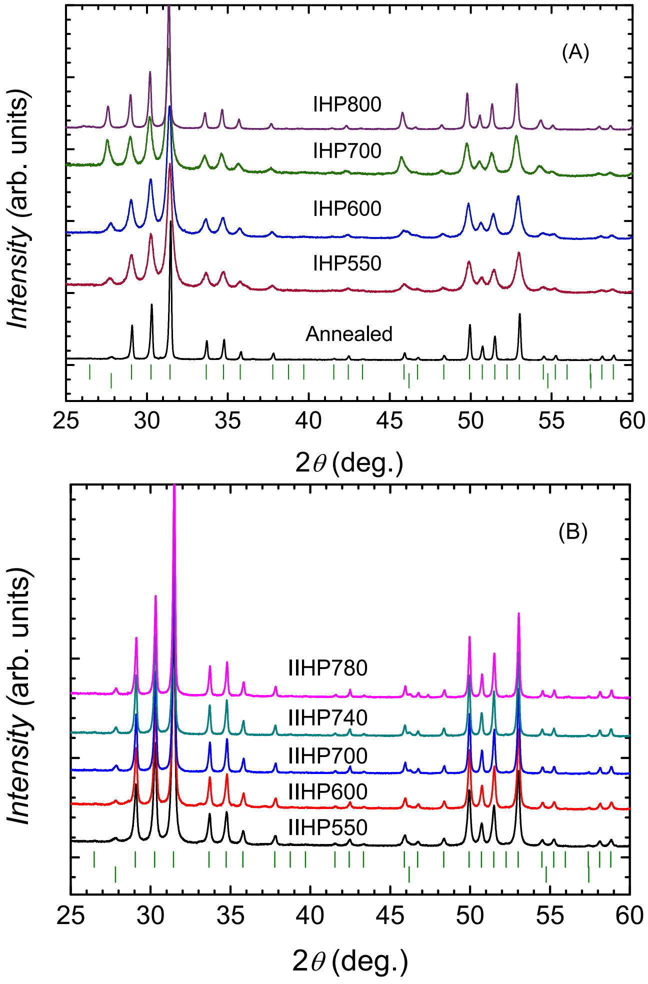

Fig. 7. Selected XPD patterns of the hot pressed samples from the IHP samples in (A) and the IIHP samples in (B).

change of the electronic band structure is generally non-linear with factors such as the Cu content [40]. The high $\rho(T)$ in the IHP samples compared to the IIHP samples is also related to the oxides on the particle surfaces (although these could not be detected by XPD and EDX) and the low bulk densities (the ratio of experimental to theoretical density). The measured composition from EDX indeed revealed the increased Cu content with increasing T_p.

In contrast, the phase composition of the IIHP samples is stable, as seen the similar lattice parameter *a* of the clathrate phase (Table 2) and similar X-ray patterns (Fig. 7(B)) in all samples. It is mainly due to the non-interrupted BM process (then less oxygen on the surface of grains) and the relatively large grains in the P-II powders. The composition of the clathrate phase measured by EDX is $Ba_8Cu_{4.6}Ge_{35.1}Si_{6.3}$ (error bar for each element: 0.1 at./u.c.), close to the nominal composition.

Such instability was also observed in samples of low bulk density at high temperatures under poor vacuum, even only for a short time, e.g. during transport measurements. Fig. 8(A) shows the XPD patterns of IIHP550, one from an as-sintered sample (denoted by IIHP550-a) and the other from the same sample but after the ρ and S measurements (denoted by IIHP550-b, T up to 600°C and the whole process lasted for 4 h). The pattern of IIHP550-b resembles those of IHP (Fig. 7(A)), with enhanced peaks for the diamond phase and shifted peaks for the clathrate phase compared to IIHP550-a. The peaks from the clathrate phase are also pronouncedly broadened (even split at high angles), as seen in the inset of Fig. 8(A). This means that, similar to the IHP sample the relative Cu content is enhanced by the loss of Ge/Si in the clathrate phase because of an oxygen induced local decomposition due to the low vacuum condition in the measurement device. This conjecture should be tested in future by high temperature measurements under high vacuum or clean inert gas atmosphere. This decomposition leads to a change of the transport properties, as shown in Fig. 8(B) (a and b): For the low bulk density samples IHP550 and IIHP550 (around 70% for both samples), $\rho(T)$ is clearly very different for the second measurement run. In contrast, the well compacted sample IIHP760 (around 99%) undergoes no composition change during measurements at high T, as evidenced by the excellent reproducibility of $\rho(T)$ data (Fig. 8(B) (b)).

4. Discussion

Our results reveal that very fine powders can be obtained in Si/Ge based clathrates by the ball milling process but the grain size largely depends on the agglomeration of powders. No decomposition occurs during this process. It is generally known that the grain size and other properties such as impurities in nano-powders influence the sintering behavior during the solidification process [32,33]: Small grains and pure grain surfaces favour the powders sintering, making the process fast and the bulk density high. However, IHP samples sintered from finer powders P-I do NOT show such a trend, in contrast, these samples have lower densities than the IIHP samples synthesized under the same hot pressing conditions (Table 2). This might be due to powder surface contaminations and local/partial decomposition induced by adsorbed oxygen consuming the surface energy in the first series of samples.

As seen in the properties of the series of IHP samples, although we can obtain samples with very low grain sizes (as low as ~25 nm), the role of the Cu content and thus of the charge carrier type and concentration still dominates the transport properties. A stable phase composition with an optimized Cu content, a high bulk density, and intermediate grain sizes would be sufficient to optimize the TE performance in Cu containing Si/Ge-based clathrates.

5. Conclusions

In summary, we have presented the effects of process

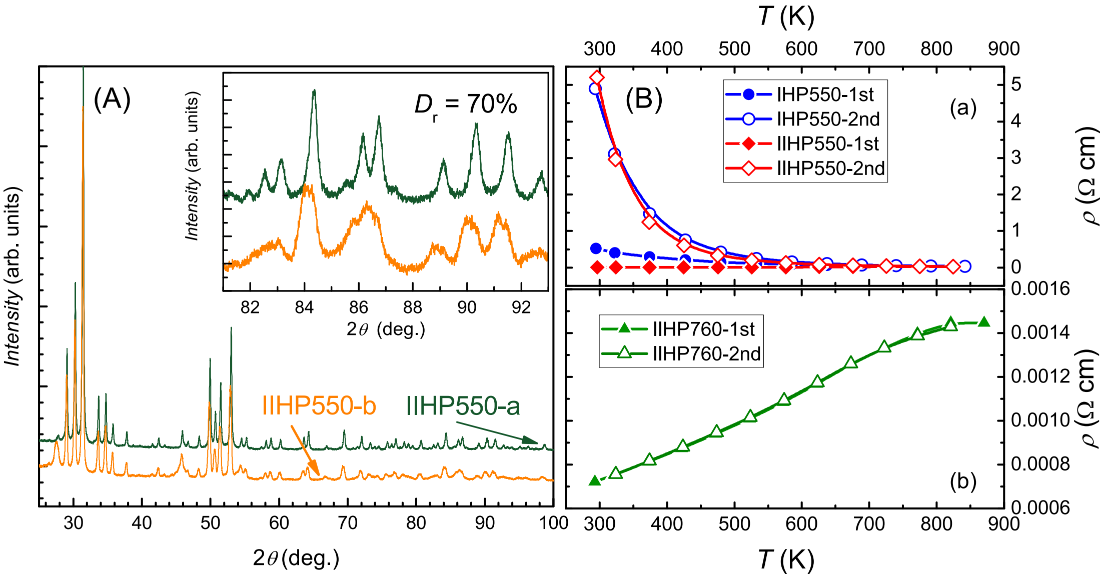

Fig. 8. (A) XPD patterns for IIHP550-a (as sintered) and IIHP550-b (experienced high *T* during transport measurement); inset, zoom in patterns in 81 – 94° and (B) the $\rho(T)$ for (a) the samples IHP550 and IIHP550 and (b) IIHP760 for two different runs on the very same sample. $\rho(T)$ of the dense sample IIHP760 is well reproduced.

parameters for ball milling (BM) and hot pressing (HP) on the chemical and transport properties of the type-I clathrate $Ba_8Cu_{4.5}Si_6Ge_{35}$. Our results reveal that very fine nanopowders can be produced by ball milling but the minimal grain size is limited by powder agglomeration effects. Very small grains with large surfaces may adsorb oxygen during the BM process in particular if opened repeatedly to reduce agglomeration, which leads to an oxygen-induced partial phase decomposition during the HP process. The decomposition apparently releases some Ge/Si from the clathrate phase and thus increases the relative Cu content. Together with the possible oxides on the grain surfaces, this phase instability deteriorates the thermoelectric performance. Such decomposition is also likely to occur in bulk samples of low density when a certain amount of oxygen exists as for instance in transport measurements at high temperatures under poor vacuum conditions. Thus, to optimize the thermoelectric properties of clathrate by nanostructuring, it is mandatory to retain a stable composition in all material synthesis processes.

Acknowledgements

The authors would like to thank F. Falmbigl and A. Grytsiv for hot pressing and M. Waas for the SEM/EDX investigation. This work was supported by the Austrian Science Fund (FWF project TRP 176-N22) and the German Science Fund (DFG SPP 1386 project nanOcla).

References

[1] X. Shi, L. Chen, C. Uher, Recent advances in high-performance bulk thermoelectric materials, Int. Mater. Rev. 61 (6) (2016) 379–415.
[2] E.S. Toberer, L.L. Baranowski, C. Dames, Advances in thermal conductivity, Annu. Rev. Mater. Res. 42 (1) (2012) 179–209.
[3] H. Alam, S. Ramakrishna, Nanostructured Thermoelectric Materials: Current Research and Future Challenges, Wiley-VCH Verlag GmbH & Co. KgaA, 2017, pp. 507–546.
[4] M. Adachi, S. Fujiif, M. Kiyama, Y. Yamamoto, T. Takeuchi, Control of nano structure by multi films for nano-structured thermoelectric materials, SEI Tech. Rev. 84 (2017) 151–155.
[5] J. Mao, Z. Liu, Z. Ren, Size effect in thermoelectric materials, npj Quantum Mater. 1 (2016), 16028 1–9.
[6] Q. Jiang, J. Yang, Y. Liu, H. He, Microstructure tailoring in nanostructured thermoelectric materials, J. Adv. Dielectr. 06 (01) (2016), 1630002 1–16.
[7] G.A. Slack, New Materials and Performance Limits for Thermoelectric Cooling, CRC Press, Boca Raton, 1995.
[8] J.L. Cohn, G.S. Nolas, V. Fessatidis, T.H. Metcalf, G.A. Slack, Glasslike heat conduction in high-mobility crystalline semiconductors, Phys. Rev. Lett. 82 (1997) 779–782.
[9] G.S. Nolas, T.J.R. Weakley, J.L. Cohn, R. Sharma, Structural properties and thermal conductivity of crystalline Ge clathrates, Phys. Rev. B 61 (2000) 3845–3850.
[10] G.S. Nolas, B.C. Chakoumakos, G.J.L.B. Mathieu, T.J.R. Weakley, Structural characterization and thermal conductivity of Type-I Tin clathrates, Chem. Mater 12 (2000) 1947–1953.
[11] G.S. Nolas, G.A. Slack, S.B. Schujman, in: Semiconductors and Semimetals, vol. 69, Academic, San Diego, CA, 2001.
[12] A.V. Shevelkov, Thermoelectric power generation by clathrates, in: S. Skipidarov, M. Nikitin (Eds.), Thermoelectrics for Power Generation – a Look at Trends in the Technology, InTech, Rijeka, 2016. Ch. 10.
[13] A. Bhattacharya, S. Bhattacharya, Unraveling the role of vacancies in the potentially promising thermoelectric clathrates $Ba_8Zn_xGe_{46-x-y}v_y$, Phys. Rev. B 94 (2016), 094305 1–6.
[14] Y. Liu, Q. Xi, J. Zhou, T. Nakayama, B. Li, Phonon-glass dynamics in thermoelectric clathrates, Phys. Rev. B 93 (2016), 214305 1–7.
[15] M. Christensen, A.B. Abrahamsen, N.B. Christensen, F. Juranyi, N.H. Andersen, K. Lefmann, J. Andreasson, C.R.H. Bal, B.B. Iversen, Avoided crossing of rattler modes in thermoelectric materials, Nat. Mater. 7 (2008) 811–815.
[16] H. Euchner, S. Pailhès, L.T.K. Nguyen, W. Assmus, F. Ritter, A. Haghighirad, Y. Grin, S. Paschen, M. de Boissieu, Phononic filter effect of rattling phonons in the thermoelectric clathrate $Ba_8Ge_{40+x}Ni_{6-x}$, Phys. Rev. B 86 (2012), 224303 1–9.
[17] S.M. Kauzlarich, S.R. Brown, G.J. Snyder, Zintl phases for thermoelectric devices, Dalton Trans. 2007 (2007) 2099–2107.
[18] E.S. Toberer, A.F. May, G.J. Snyder, Zintl chemistry for designing high efficiency thermoelectric materials, Chem. Mater. 22 (2010) 624–634.
[19] M. Falmbigl, A. Grytsiv, P. Rogl, P. Heinrich, E. Royanian, E. Bauer, Tuning of band gap and thermoelectric properties of type-I clathrate $Ba_8Ni_xZn_yGe_{46-x-y-z}Sn_z$, J. Alloys Compd. 567 (2013) 65–72.
[20] A. Saramat, G. Svensson, A.E.C. Palmqvist, C. Stiewe, E. Mueller, D. Platzek, S.G.K. Williams, D.M. Rowe, J.D. Bryan, G.D. Stucky, Large thermoelectric figure of merit at high temperature in Czochralski-grown clathrate $Ba_8Ga_{16}Ge_{30}$, J. Appl. Phys. 99 (2) (2006), 023708 1–5.
[21] H. Zhang, H. Borrmann, N. Oeschler, C. Candolfi, W. Schnelle, M. Schmidt, U. Burkhardt, M. Baitinger, J.-T. Zhao, Y. Grin, Atomic interactions in the p-type clathrate I $Ba_8Au_{5.3}Ge_{40.7}$, Inorg. Chem. 50 (4) (2011) 1250–1257.
[22] J. Xu, J. Wu, H. Shao, S. Heguri, Y. Tanabe, Y. Liu, G.-Q. Liu, J. Jiang, H. Jiang, K. Tanigaki, Structure and thermoelectric properties of the n-type clathrate $Ba_8Cu_{5.1}Ge_{40.2}Sn_{0.7}$, J. Mater. Chem. A 3 (2015) 19100–19106.
[23] L.T.K. Nguyen, U. Aydemir, M. Baitinger, E. Bauer, H. Borrmann, U. Burkhardt, J. Custers, A. Haghighirad, R. Höfler, K.D. Luther, F. Ritter, W. Assmus, Y. Grin, S. Paschen, Atomic ordering and thermoelectric properties of the n-type clathrate $Ba_8Ni_{3.5}Ge_{42.1}v_{0.4}$, Dalton Trans. 39 (2010) 1071–1077.
[24] A.J. Minnich, M.S. Dresselhaus, Z. Ren, G. Chen, Bulk nanostructured thermoelectric materials: current research and future prospects, Energy Environ. Sci. 2 (2009) 466–479.

[25] E.L. Hu, D.T. Shaw, in: Nanostructure Science and Technology, Kluwer Academic Publ, Dordrecht, 1999.

[26] G.R. Kumar, K. Jayasankar, S.K. Das, T. Dash, A. Dash, B.K. Jena, B.K. Mishra, Shear-force-dominated dual-drive planetary ball milling for the scalable production of graphene and its electrocatalytic application with pd nanostructures, RSC Adv. 6 (2016) 20067−20073.

[27] V.K. Krishnan, K. Sinnaeruvadi, Synthesis of nanostructured vanadium powder by high-energy ball milling: X-ray diffraction and high-resolution electron microscopy characterization, Philos. Mag. Lett. 96 (10) (2016) 402−408.

[28] I. Marek, D. Vojtech, A. Michalcova, T.F. Kubatsek, The structure and mechanical properties of high-strength bulk ultrafine-grained cobalt prepared using high-energy ball milling in combination with spark plasma sintering, Materials 9 (5) (2016), 391 1−10.

[29] A. Miura, T. Kikkawa, R. Iguchi, K.-i. Uchida, E. Saitoh, J. Shiomi, Probing length-scale separation of thermal and spin currents by nanostructuring yig, Phys. Rev. Mater. 1 (2017), 014601 1−7.

[30] C.C. Koch, Top-down synthesis of nanostructured materials: mechanical and thermal processing methods, Rev. Adv. Mater. Sci. 5 (2003) 91−99.

[31] H.J. Fecht, Y. Ivanisenko, in: Nanostructured Materials: Processing, Properties, and Applications, William Andrew Publishing, 13 Eaton Avenue Norwich, NY 13815, 2006.

[32] J. Eckert, J. Holzer, C. Krill, W. Johnson, Structural and thermodynamic properties of nanocrystalline fcc metals prepared by mechanical attrition, J. Mater. Res. 7 (1992) 1752−1761.

[33] C. Koch, The synthesis and structure of nanocrystalline materials produced by mechanical attrition: a review, Nanostruct. Mater. 2 (2) (1993) 109−129.

[34] C.C. Koch, Synthesis of nanostructured materials by mechanical milling: problems and opportunities, Nanostruct. Mater. 9 (1−8) (1997) 13−22.

[35] F.F.C. Suryanarayana, Nanocrystalline structures from amorphous precursors, Nano Mater. 3 (1993) 147−153.

[36] J.R. Groza, in: Nanostructured Materials: Processing, Properties, and Applications, William Andrew Publishing, 13 Eaton Avenue Norwich, NY 13815, 2006.

[37] X. Yan, E. Bauer, P. Rogl, S. Paschen, Structural and thermoelectric properties of $Ba_8Cu_5Si_xGe_{41-x}$ clathrates, Phys. Rev. B 87 (2013), 115206 1−9.

[38] F.J. Blatt, Physics of Electronic Conduction in Solids, McGraw-Hill, New York, 1968.

[39] X. Yan, M. Falmbigl, G. Rogl, A. Grytsiv, A. Prokofiev, E. Bauer, P. Rogl, M. Zehetbauer, S. Paschen, High-pressure torsion to improve thermoelectric efficiency of clathrates? J. Electron. Mater. 42 (2013) 1330−1334.

[40] X. Yan, M.X. Chen, S. Laumann, E. Bauer, P. Rogl, R. Podloucky, S. Paschen, Thermoelectric properties of Ba-Cu-Si clathrates, Phys. Rev. B 85 (2012), 165127 1−10.

[41] X. Yan, M. Falmbigl, S. Laumann, A. Grytsiv, E. Bauer, P. Rogl, S. Paschen, Structural and thermoelectric properties of $Ba_8CuxSi_{23-x}Ge_{23}$ ($4.5 \leq x \leq 7$), J. Electron. Mater. 41 (2012) 1159−1164.

[42] L. Zhang, A. Grytsiv, M. Kerber, P. Rogl, E. Bauer, M. Zehetbauer, J. Wosik, G. Nauer, $MmFe_{[4]}Sb_{[12]}$- and $CoSb_3$-based nano-skutterudites prepared by ball milling: Kinetics of formation and transport properties, J. Alloys Compd. 481 (1−2) (2009) 106−115.

[43] S. Enzo, G. Fagherazzi, A. Benedetti, S. Polizzi, Profile-fitting procedure for analysis of broadened x-ray diffraction peaks: I. Methodology, J. Appl. Cryst. 21 (1998) 536−542.

[44] S. Enzo, G. Fagherazzi, A. Benedetti, S. Polizzi, Profile-fitting procedure for analysis of broadened x-ray diffraction peaks: II. Application and discussion of the methodology, J. Appl. Cryst. 21 (1998) 543−549.

[45] A. Zolriasatein, X.L. Yan, P. Rogl, A. Shokuhfar, S. Paschen, Preparation of nanocrystalline Ba-Cu-Si clathrate powders by mechanical milling using a process control agent, J. Nano. Res. 29 (2014) 121−127.

[46] S. Gaona-Jimenez, R.A. Rodriguez-Diaz, A. Sedano, J. Porcayo-Calderon, A.M. Ocampo, S. Serna-Barquera, J.O. Olarte-Cortes, J.A. Juarez-Islas, Dig. J. Nanomater. Bios. 12 (2) (2017) 449−462.